Diverse helicities of dipolar skyrmions

Lingyao Kong,[1] Jin Tang,[1,2,*] Yaodong Wu,[3] Weiwei Wang,[4] Jialiang Jiang,[2] Yihao Wang,[2] Junbo Li,[2] Yimin Xiong,[1] Shouguo Wang,[5] Mingliang Tian,[1,2] and Haifeng Du[2]

[1]*School of Physics and Optoelectronic Engineering, Anhui University, Hefei 230601, China*

[2]*Anhui Province Key Laboratory of Condensed Matter Physics at Extreme Conditions, High Magnetic Field Laboratory, HFIPS, Anhui, Chinese Academy of Sciences, Hefei 230031, China*

[3]*School of Physics and Materials Engineering, Hefei Normal University, Hefei 230601, China*

[4]*Institutes of Physical Science and Information Technology, Anhui University, Hefei 230601, China*

[5]*Anhui Key Laboratory of Magnetic Functional Materials and Devices, School of Materials Science and Engineering, Anhui University, Hefei, 230601, China*

(Received 20 July 2023; accepted 11 December 2023; published 2 January 2024)

Magnetic skyrmions, vortex-like spin textures possessing remarkable topological electron-magneto properties, have emerged as promising candidates for information storage and processing in future spintronic devices. Helicity, which characterizes the rotational sense of the spin swirl, represents a crucial degree of freedom for encoding information in magnetic skyrmions. Traditionally, states with one and two helicities have been established for skyrmions in chiral and dipolar/frustrated magnets, respectively. In this study, we explore the helicity diversity of dipolar skyrmions in centrosymmetric magnets by extending our investigation to three-dimensional uniaxial magnetic systems. Combining numerical simulations, we demonstrate that the inclusion of additional spin twists along the depth dimension expands the twofold helicity degeneracy to fourfold and potentially beyond. Our findings not only provide insights into the spin models of dipolar skyrmions but also promote the development of topological spintronic devices, leveraging helicity as a key parameter.

DOI: 10.1103/PhysRevB.109.014401

I. INTRODUCTION

Magnetic skyrmions are topological spin swirls that are potentially applicable for topological spintronic devices [1–9]. These skyrmions are characterized by three freedom parameters: vorticity, polarity, and helicity [3]. The helicity, denoted as h, describes the rotation sense of the skyrmionic swirl and can be expressed as the angle between the in-plane magnetization and the radial axis from the vortex center. In specific cases, Bloch skyrmions and Neel skyrmions exhibit helicity values of $h = 0,\ \pi$, and $h = \pm\pi/2$, respectively [10,11]. However, skyrmions with helicity values different from these are referred to as hybrid Bloch-Neel skyrmions [12,13]. These distinct types of skyrmions with varying helicity values contribute to the richness and versatility of skyrmion-based systems, offering opportunities for tailoring their properties to specific technological applications [14–17].

In noncentrosymmetric magnets, skyrmions stabilized by the Dzyaloshinskii-Moriya interaction (DMI) exhibit a locked relationship between helicity and polarity, also known as chirality [1]. The polarity is determined by the orientation of the out-of-plane magnetic field, resulting in a single style of helicity for chiral skyrmions. Conversely, in centrosymmetric magnets where skyrmions are stabilized by dipolar interactions or frustration effects, the absence of chiral interactions leads to a twofold degeneracy in skyrmion helicity [18,19]. The helicity can determine the dynamics of skyrmions, and becomes an important freedom parameter for information coding in topological spintronic devices [12,17,20]. Moreover, recent studies explore the potential of the twofold helicity of skyrmions for quantum-qubit applications [16,18]. Both experiments and simulations have proposed various techniques, including current [17], voltage [21], and thermal methods [22], to control skyrmion helicity. A comprehensive understanding of skyrmion helicity is crucial for the development of helicity-based topological spintronic devices.

In the pursuit of developing three-dimensional (3D) topological solitons, such as skyrmion bundles [23], bobbers [24], and Hopfions [25], the consideration of magnetism in the depth dimension provides an additional spatial degree of freedom. Recent studies have uncovered intriguing phenomena, including complex Bloch-to-Neel helicity reversal, occurring from the interior to the surface layers of uniaxial magnets and magnetic multilayers [26–28]. These reversals are attributed to the influence of magnetic dipolar-dipolar interactions. Notably, despite the presence of additional spin twists along the depth orientation, dipolar skyrmions in uniaxial magnets still maintain a twofold degeneracy in helicity [19,26,29]. Here, we refer to dipolar skyrmions and bubbles in Fe_3Sn_2 as the spin configurations with $Q = -1$ and 0, respectively. Moreover, in our previous work [30], we have also presented a hybrid skyrmion-bubble configuration, in which the magnetizations in near-surface and middle layers possess $Q = -1$ and 0, respectively.

In this study, combining 3D micromagnetic simulation with Lorentz transmission electronic microscopy magnetic imaging, we investigate the multifold freedom of spin twists

*Corresponding author: jintang@ahu.edu.cn

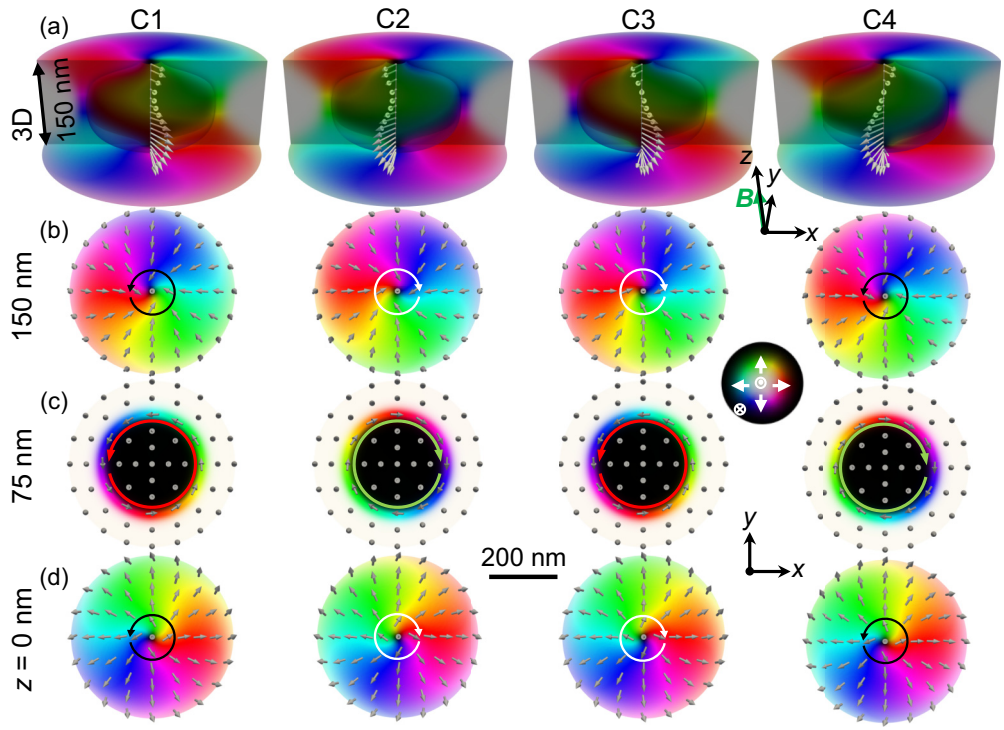

FIG. 1. Simulated 3D dipolar skyrmions with a diverse helicity. (a) 3D and cross-sectional spin configurations, (b) magnetizations in the top surface layer $z = 150$ nm, (c) magnetizations in the middle layer $z = 75$ nm, and (d) magnetizations in the bottom surface layer $z = 0$ nm for four types of dipolar skyrmions denoted by C1, C2, C3, and C4. Black and red annular arrows represent a counterclockwise rotation of the Bloch spin twists, while white and green ones denote a clockwise rotation of the Bloch spin twists. The color scheme signifies the magnetization orientation, according to the color wheel. The arrows in (a) are plotted on the isosurface $m_z = -0.5$. Magnetic field is 200 mT.

along the depth in a centrosymmetric uniaxial magnet Fe_3Sn_2 [26,30–33]. Our findings demonstrate the presence of Bloch-twisted skyrmions in the interior layers, while hybrid Bloch-Neel-twisted skyrmions are observed in the near-surface layers. Notably, the integrated magnetizations over the top and bottom layers exhibit residual Bloch spin twists, which can align and antialign with the helicity of skyrmions in the interior layer. Consequently, the degeneracy of 3D dipolar skyrmions can be expanded from a twofold to a fourfold and potentially higher-fold degeneracy. These results promote the fundamental understanding of spin textures of dipolar skyrmions, and potential spintronic device applications based on helicity.

II. METHOD

We use *in situ* Lorentz TEM (Talos F200X, FEI) at 200 kV to image Fe_3Sn_2 films (3.4 μm × 4.2 μm, 150 nm thickness). The differential phase contrast (DPC) microscope is operated at low magnification in scanning TEM (STEM) mode using a split quadrant detector. The probe convergence and detection angles for the DPC-STEM measurements are set to 7 and 1 mrad, respectively; the corresponding probe size is 3.6 nm. All experiments are performed at room temperature. The Fe_3Sn_2 disks are fabricated from a single crystal employing a focused ion beam and scanning electron microscopy (Helios Nanolab 600i, FEI). Single crystals are grown via chemical vapor transport with high-purity iron and tin. Fe_3Sn_2's out-of-plane orientation is the [001] axis identified by x-ray diffraction. A heating process (800°C for 7 days), followed by grinding and temperature gradient maintenance (720°C to 650°C for 2 weeks) are employed to prepare sintered Fe_3Sn_2. The ion-sputtered carbon disk is transferred to a copper grid for TEM magnetic imaging. Further specifics regarding the disk fabrication process are outlined in previous reports [34,35]. Micromagnetic simulations with the double precision GPU acceleration (MUMAX3 [36], JUMAG [37]), consider exchange interaction (A), magnetic anisotropy (K_u), and dipole-dipole interaction at room temperature ($K_u = 54.5\,\mathrm{kJm^{-3}}$, $M_s = 622.7\,\mathrm{kAm^{-1}}$, $A = 8.25\,\mathrm{pJ\,m^{-1}}$ [26,32]). To characterize the properties of isolated dipolar skyrmions, a disk geometry with 510-nm diameter, 150-nm thickness, and a cell size of $3 \times 3 \times 3\,\mathrm{nm^3}$ is used in the simulations. Simulated Fresnel contrasts are obtained utilizing a modified MALTS tool [38].

III. RESULTS AND DISCUSSION

Magnetic dipolar skyrmions, also referred to as type-I bubbles or skyrmion bubbles, are a result of the delicate balance between uniaxial anisotropies and magnetic dipole-dipole interactions [19,26,29,39–46]. These are commonly found in centrosymmetric uniaxial magnets. Typically, dipolar skyrmions are represented by cylindrical domains with magnetizations that are antiparallel to out-of-plane orientations and closure domain walls, which contribute to an integer charge Q. This is evidenced by the magnetization in the middle layers of 3D dipolar skyrmions in Fe_3Sn_2, as illustrated

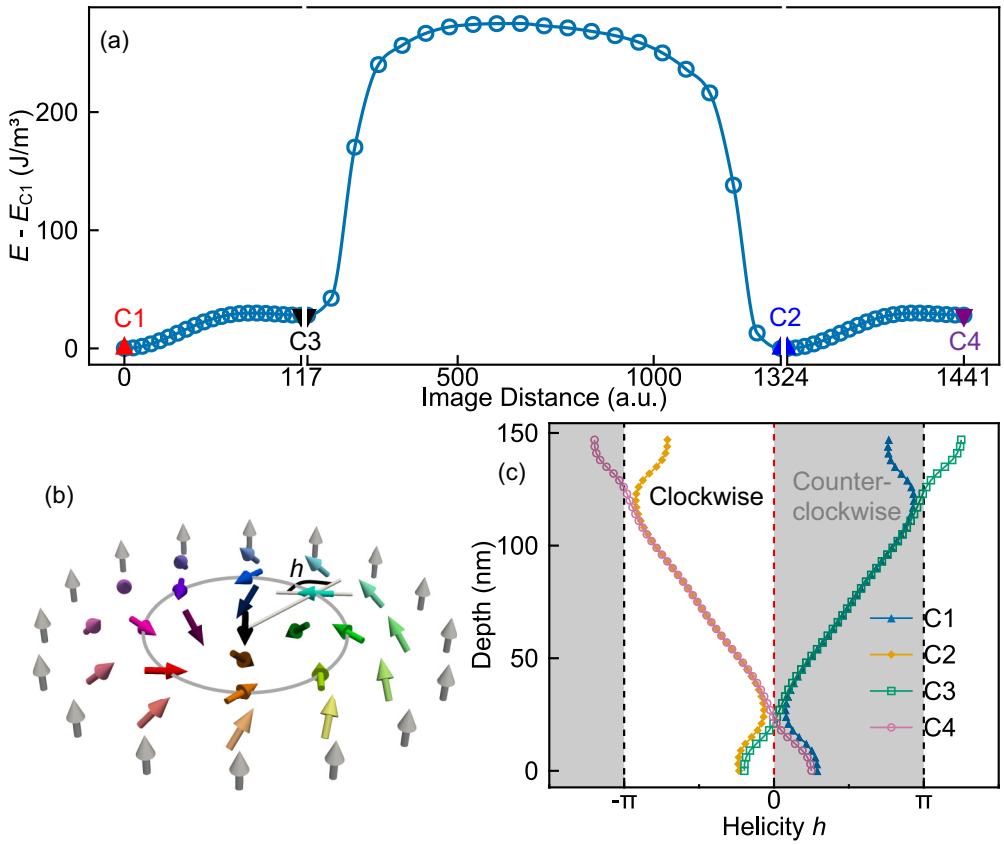

FIG. 2. (a) The mutual transformation from C1 to C3, subsequently to C2, and finally to C4. The uniquely marked symbols correspond to the stable equilibrium states as depicted in Fig. 1. (b) Schematic representation describing the helicity h. (c) The corresponding helicity h along the depth for four configurations.

in Fig. 1. Sharing identical topology, topological electromagnet properties, and nanometric room-temperature size with chiral skyrmions, dipolar skyrmions exhibit twofold degenerate rotation senses of domain wall magnetization, either clockwise or counterclockwise [19,26,29,39,40,42–46]. Based on measured magnetic parameters of Fe_3Sn_2 [19,26,39], we simulated 3D spin textures therein using MUMAX3 [36]. In 3D uniaxial magnets, the magnetizations are not uniform in depth due to the magnetic dipole-dipole interactions. These dipole-dipole interactions cause the spin twists in the near-surface layers to follow the Neel-type rule. Furthermore, the competition between ferromagnetic exchange interaction and dipole-dipole interaction results in hybrid Bloch-Neel spin twists in near-surface layers, demonstrated by the magnetizations in near-surface layers in Figs. 1(b) and 1(d). The helicity of the Bloch-twisted component in near-surface layers typically aligns with that in the middle layers. We employ the notations C1 and C2 to denote the counterclockwise and clockwise rotations of 3D dipolar skyrmions in all layers, respectively. Notwithstanding the additional spin twists along the depth, the topological charge Q in each layer remains -1.

Setting skyrmions with C1 and C2 helicities as two end states, we obtain their mutual transformation using a nudged elastic band (NEB) [37] simulation, as illustrated in Fig. 2(a). Interestingly, the NEB simulations identify an additional metastable skyrmionic phase denoted as C3, as shown in Fig. 1. Here, we define the helicity angle h as the angle between the in-plane magnetization and the radial axis from the skyrmion center, as shown in Fig. 2(b). While the helicity of the middle layer for the C3 skyrmion ($h = \pi/2$) mirrors that of the C1 skyrmion, the spin twists in their near-surface layers rotate differently. For the C3 skyrmion, the helicity angles at the top and bottom surface layers are $h > \pi$ and $h < 0$ [Fig. 2(b)], respectively. Consequently, for the C3 skyrmion, the Bloch components of hybrid skyrmions in near-surface layers exhibit clockwise rotations [Figs. 1(b) and 1(d)], in contrast to the counterclockwise rotations of skyrmions in the middle layers [Fig. 1(c)]. Based on symmetry, a skyrmion phase with C4 helicity also exists, where the Bloch-component spin twists in the surface and middle layers display clockwise and counterclockwise rotations, respectively, as depicted in Fig. 1. The spin twists for C1 and C3 skyrmions reveal identical helicities in the interior layers [Fig. 2(c)], i.e., $z = 30$–75 nm, with $h \in [0, \pi/2]$. Upon reaching the surface layers, the spin twists have two options, resulting in the formation of C1 and C3 skyrmions. The magnetic transformation from C1 to C2 skyrmions comprises two stages mediated by the C3 skyrmions (Fig. 2(a) and Supplemental Fig. S1 [47]): (1) The residual Bloch-twisted spins in the surface layers switch from clockwise ($h = 2.41$ in the top surface and 0.91 in the bottom surface) to counterclockwise ($h = 3.93$ in the top surface and -0.62 in the bottom surface) rotations, in the range of image distance from 0 to 117; (2) The

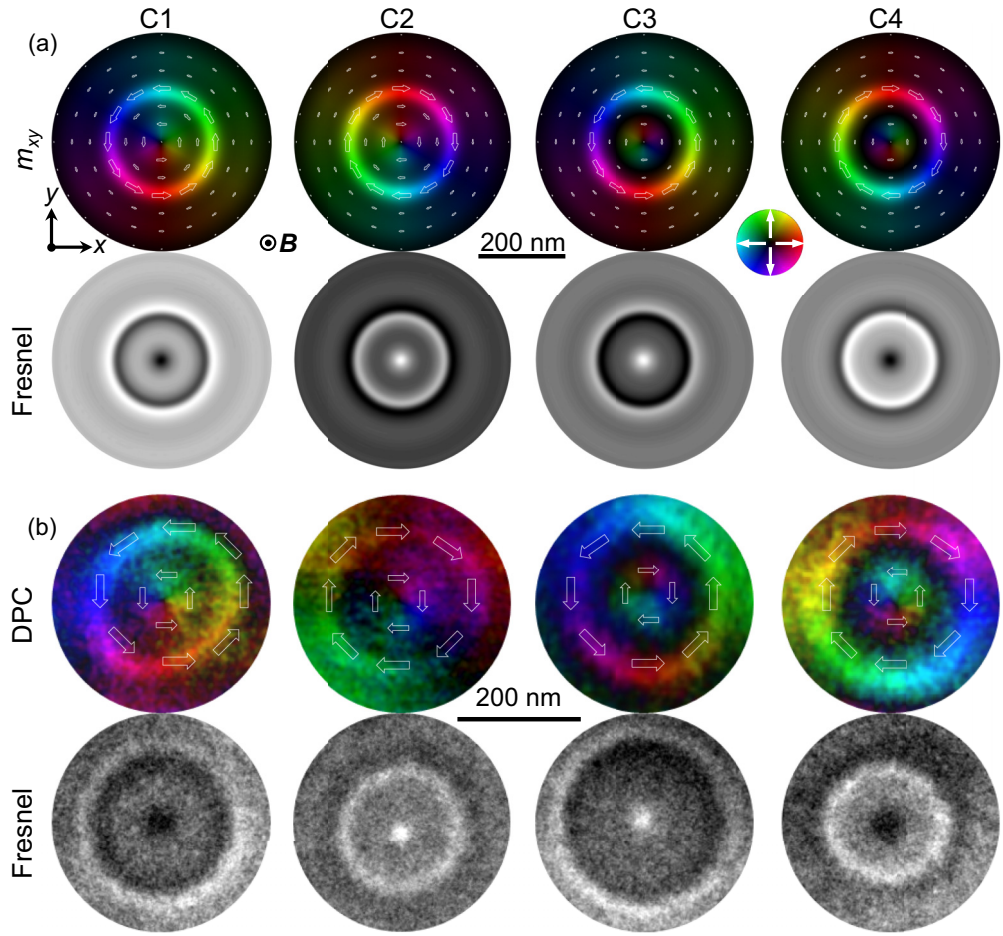

FIG. 3. Observation of dipolar skyrmions with fourfold degeneration in Fe_3Sn_2. (a) Simulated average in-plane magnetization mappings, with the following corresponding under-defocused Fresnel images. (b) Experimental DPC magnetization images, with the following corresponding under-defocused Fresnel image. The color indicates the in-plane magnetization orientation and magnitude based on the color wheel. Defocused distance, −500 μm.

Block-component twisted spins in the middle layers transition from clockwise ($h = 1.53$ in the middle) to counterclockwise ($h = 5.7$ in the middle) rotations, in the range of image distance from 117 to 1324. Similarly, the inverse magnetic transformation from C2 to C1 skyrmions should also include two steps mediated by the C4 skyrmions [Fig. 2(a)].

Three-dimensional C1 and C2 dipolar skyrmions have been widely experimentally identified from the two-dimensional (2D) average in-plane magnetization [10,17,22,26,29,40,43–46]. The NEB calculations demonstrate that the energy barrier required for the transformation from C3 to C2 is 4.7×10^{-20} J, while transitioning from C2 to C4 necessitates an energy barrier of 7.6×10^{-18} J. Both barriers significantly surpass the thermal fluctuation energy $k_BT = 4 \times 10^{-21}$ J (k_B is the Boltzmann constant) at room temperature ($T = 290$ K), thereby suggesting the potential stabilities of C3 and C4 skyrmion at room temperature. We further calculate the magnetic configurations initialized by C1 and C3 states after a 1-ns relaxation at $T = 300$ K (Supplemental Fig. S2 [47]). Our results provide evidence for the stability of these states at room temperature. Our calculations also demonstrate that all four states can remain stable for thicknesses exceeding 130 nm (Supplemental Fig. S3 [47]).

In the surface layers of dipolar skyrmions, the Bloch component primarily originates from the near-center region, whereas in the middle layer, the helicity is concentrated in an outer ring, as indicated by the white dotted arrows in Fig. 1(b). Therefore, the diverse helicities are distributed across different in-plane regions, suggesting that Lorentz TEM could effectively distinguish these different helicities [48]. To further analyze the distribution of helicities along the depth of the C3 and C4 skyrmion configuration, we investigate the average in-plane magnetization and corresponding under-defocused Fresnel images for different z regions, as detailed in Fig. 3 and Supplemental Fig. S4 [47]. The near-surface layers at $z = 0 - 45$ nm and $z = 105$–150 nm contribute to the signal at the center of the Fresnel image, while the middle layers at $z = 45$–105 nm contribute to the signal on the outer ring. Upon averaging over the top and bottom near surfaces, the Neel component of the in-plane magnetization cancels out, yielding a corresponding Fresnel image that displays a counterclockwise (clockwise) rotation in the center and a clockwise (counterclockwise) rotation on the outer ring for C3 (C4) (Supplemental Fig. S4 [47]). Figure 3(a) presents the simulated average in-plane magnetization mapping for the four configurations, where the helicity near the center is

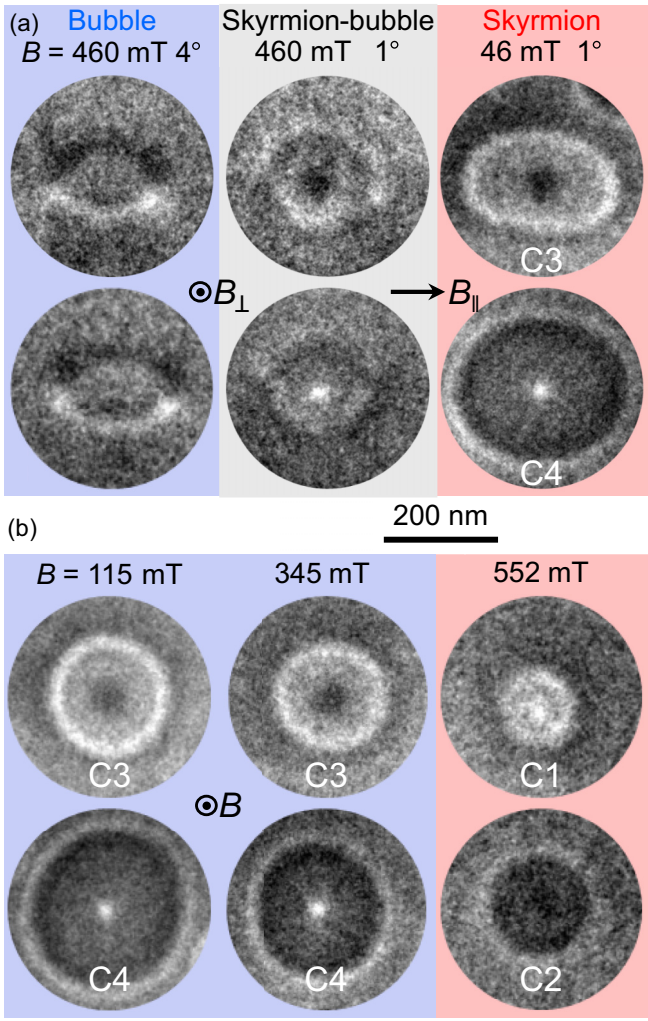

FIG. 4. (a), Bubble-to-skyrmion transformation with decreasing titled field angle β, and then decreasing magnetic field. The orientation of the in-plane field component $B_{\parallel}$ is depicted by the black arrow. (b) C3-to-C1 and C4-to-C2 skyrmion transformation in the field-increasing process at a field angle $\beta = 0$. Defocused distance, $-500\,\mu$m.

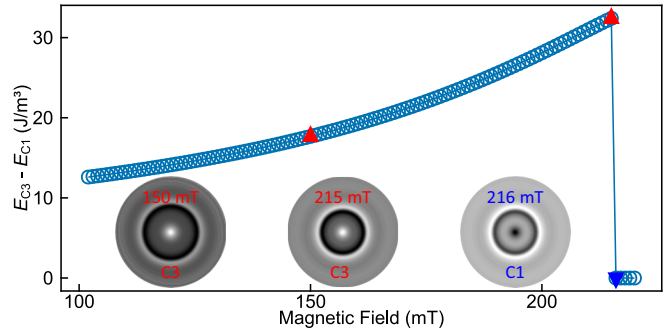

FIG. 5. Simulated magnetic field-dependent total energy density difference between initialized with C3 to C1 skyrmions $E_{C3} - E_{C1}$.

inverted compared to that of the outer rings that show up on C3 and C4 structures. The Fresnel Lorentz TEM method is sensitive to the Bloch spin twists of vortex-like structures [48], which manifests as the Lorentz scattering of probe electrons. As a result, a strengthened (brightness) and weakened (darkness) target-like pattern is observed in Fresnel Lorentz TEM images corresponding to clockwise and counterclockwise rotations, respectively.

Here, we employ both Fresnel and DPC scanning transmission electron microscopy magnetic imaging techniques, which visualize the in-plane magnetizations [26,32,49,50], to identify the diversity of helicities, as shown in Fig. 3. Figure 3(b) displays the experimental DPC and Fresnel images, which closely resemble the corresponding simulated configurations shown in Fig. 1. This offers ambiguous experimental proof for the diversity of helicities for dipolar skyrmions.

Notably, the dipolar skyrmions exhibiting a diversity of helicities [Fig. 3(b)] could be easily misinterpreted as 2π skyrmions [34], without accounting for 3D magnetism. However, a crucial distinction between 2π skyrmions and dipolar skyrmions with varied helicities lies in their disparate topological charges. While 2π skyrmions carry a topological charge of $Q = 0$, dipolar skyrmions hold a charge of $Q = -1$. Due to the absence of the DMI, dipolar skyrmions permit both rotations. As a result, the detection of the center and one outside ring pattern in the images of dipolar skyrmions exhibiting fourfold helicity aligns with this characteristic.

Skyrmions with C1 and C2 helicities have been frequently obtained experimentally in uniaxial magnets. In this work, we achieved the experimental realization of skyrmions with C3 and C4 helicities through a process involving a tilted field at a low field region, as depicted in Fig. 4(a). At high tilted field angles, topologically trivial bubbles with $Q = 0$ always remain stable to minimize Zeeman energy [30,45]. By decreasing the field angle to 1° at $B = 460$ mT, the bubble initially transforms to a hybrid skyrmion-bubble, which consists of skyrmions in the near-surface layers and bubbles in the interior layers [30]. Then, with decreasing the field to $B = 46$ mT, the hybrid skyrmion-bubble finally transforms to a dipolar skyrmion accompanied by the annihilation of Bloch lines in the interior layers (see Supplemental Fig. S5 for detailed simulated structures [47]). The topological magnetic transformation from a bubble to a skyrmion proceeds in two steps: (1) Bubbles in the near-surface layers transform into hybrid Bloch-Neel-twisted skyrmions at a relatively high tilted angle; (2) Bubbles in the interior layers transform into Bloch-twisted skyrmions at a relatively low tilted angle. During the transformation of the second step, the helicity of Bloch spin twists in the middle layers has two options, either align or antialign with the Bloch component of spin twists in the near-surface layers. The latter option leads to the formation of dipolar skyrmions with C3 and C4 helicities.

We further investigate the stability of dipolar skyrmions with C3 and C4 helicities under increasing magnetic fields, as depicted in Fig. 4(b). As the magnetic field increases to about 552 mT, the C3/C4 skyrmion becomes unstable and transforms to a C1/C2 skyrmion, demonstrated by the transition of the center helicity from bright to dark in the Fresnel images [Fig. 4(b)]. The major transformations occur in near-surface layers, leading to a change in the central magnetic contrasts of dipolar skyrmions. To explain the stability of skyrmions with C3 and C4 helicities, we perform simulations that trace the magnetic evolution under an increasing

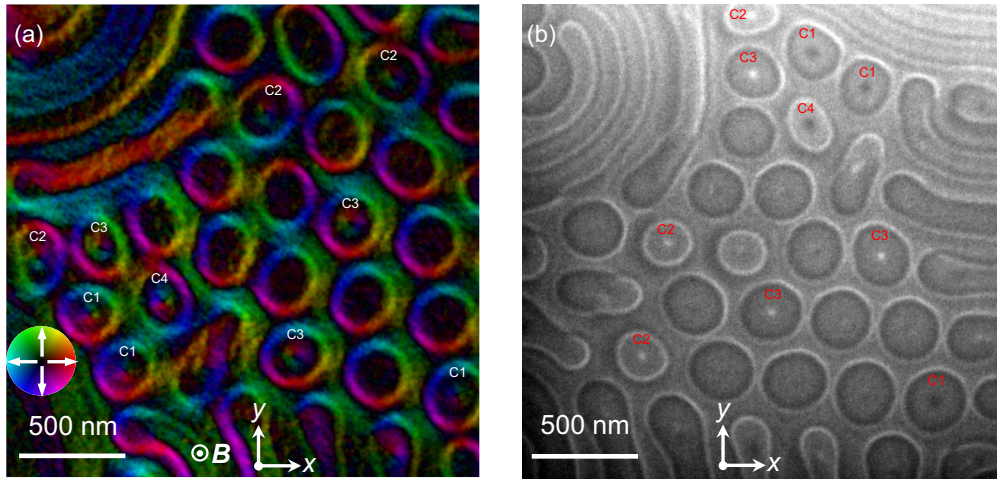

FIG. 6. Observation of dipolar skyrmions at a large Fe_3Sn_2 lamella. (a), DPC magnetization image under external magnetic field of 46 mT. The color scheme signifies the magnetization orientation, according to the color wheel. (b), Fresnel image under zero field. Defocused distance, −500 μm.

magnetic field, starting with an initial C3 skyrmion (Fig. 5 and Supplemental Fig. S6 [47]). The C3 skyrmion remains stable, yet it undergoes a transformation to a C1 skyrmion when the magnetic field surpasses 215 mT, with the helicity in the near-surface layers experiencing an abrupt shift. The high-field instability of C3 and C4 skyrmions suggests that a small titled field angle, approximately around 1°, is a crucial factor in the field-decreasing process [Fig. 4(a)]. This small angle enables the transformation of these skyrmions into C3 and C4 configurations at low magnetic fields, originating from their hybrid skyrmion-bubble states observed at high fields.

The helicity angles for both the top surface ($h = -0.78$ to -0.62) and bottom surface ($h = 4.06$ to 3.93) exhibit slow alterations when the field ascends from 100 mT to 215 mT. A sudden change from $h = -0.48$ to 0.92 is observed on the top surface and from $h = 3.79$ to 2.41 on the bottom surface upon reaching the critical transformation field $B = 215$ mT. The simulated C3-to-C1 skyrmion transformation (Fig. 5 and Supplemental Fig. S6 [47]) is quite consistent with our observations [Fig. 4(b)]. While the energies for the C3 and C4 skyrmions are slightly higher than those of C1 and C2 skyrmions, the energy difference gets much smaller in the region of lower fields (Fig. 5), thereby rationalizing the stabilization of C3 and C4 skyrmions in lower magnetic fields.

In addition to the skyrmions with C1–C4 helicities, as displayed in Fig. 6, there are more skyrmions without central vortex-like spin configurations. This suggests a higher-fold degeneracy of helicity. Herein, we introduce dipolar skyrmions with four additional helicities of the hybrid states, as illustrated in Supplemental Fig. S7 [47]. These hybrid states exhibit spin twists in the Bloch component in the top surface layer that can be reversed with those in the bottom surface. With the dual helicity of Bloch skyrmions in the middle layers, these hybrid structures can exhibit a fourfold helicity. For

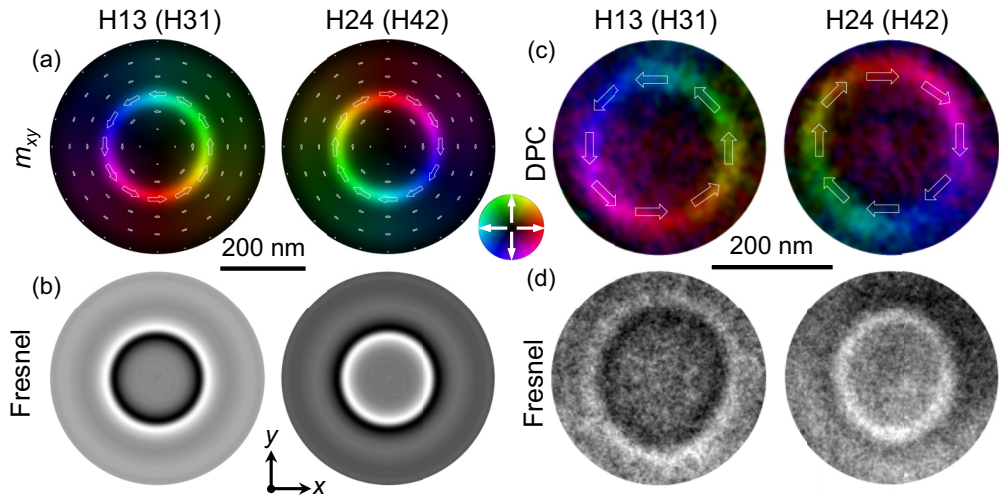

FIG. 7. Observation of dipolar skyrmions of four hybrid configurations in Fe_3Sn_2. (a) Simulated average in-plane magnetization mappings, (b) simulated under-defocused Fresnel images, (c) experimental DPC image, and (d) experimental under-defocused Fresnel image. The color scheme signifies the magnetization orientation, according to the color wheel. Defocused distance, −500 μm.

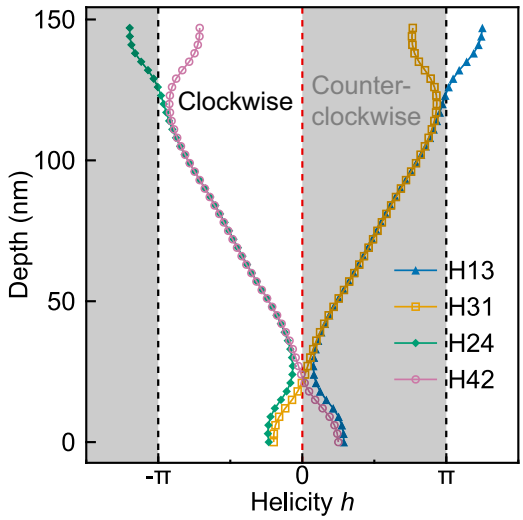

FIG. 8. The corresponding helicity h along the depth for four hybrid configurations.

instance, H13 represents the hybrid state of the bottom layers of C1 and the top layers of C3, and this nomenclature extends to H31, H24, and H42 states. Due to the reverse rotation of the Bloch components at the top and bottom surface layers for these hybrid states, the overall in-plane magnetization, when integrated with the two proximate surface layers, completely cancels out, resulting in zero in-plane magnetizations and Fresnel contrasts (Figs. 7 and 8). Consequently, H13 and H31, as well as H24 and H42, exhibit identical in-plane magnetization mappings and Fresnel contrasts, making it challenging to distinguish them using traditional Lorentz TEM. Our experiments also confirm the presence of hybrid skyrmions lacking central Fresnel contrasts [Figs. 7(c) and 7(d)], showcasing the diverse multifold freedom of helicities in dipolar skyrmions.

IV. CONCLUSIONS

In summary, we have demonstrated the theoretical prediction and experimental observation of 3D dipolar skyrmions with diverse helicities in Fe_3Sn_2 nanostructures. The magnetic dipole-dipole interaction induces additional spin twists along the depth orientation, enabling the multifold freedom helicities for skyrmions in near-surface and interior layers. By extending the 3D topological spin twists, we achieve a fourfold, and potentially even greater, degeneracy of helicity through a two-step magnetic reversal from bubbles. Our results reveal the diverse helicities in dipolar skyrmions, suggesting this could be a significant variable for information encoding in future topological spintronic devices.

ACKNOWLEDGMENTS

This work was supported by the National Key R&D Program of China, Grant No. 2022YFA1403603; the Natural Science Foundation of China, Grants No. 12174396, No. 12104123, No. 11974021, No. 12374098, and No. 12241406; the National Natural Science Funds for Distinguished Young Scholars, Grant No. 52325105; the Anhui Provincial Natural Science Foundation, Grant No. 2308085Y32; the Natural Science Project of Colleges and Universities in Anhui Province, Grant No. 2022AH030011; and the Innovation Program for Quantum Science and Technology, Grant No. 2021ZD0302802.

[1] A. Bogdanov and A. Hubert, Thermodynamically stable magnetic vortex states in magnetic crystals, J. Magn. Magn. Mater. **138**, 255 (1994).

[2] S. Mühlbauer, B. Binz, F. Jonietz, C. Pfleiderer, A. Rosch, A. Neubauer, R. Georgii, and P. Böni, Skyrmion lattice in a chiral magnet, Science **323**, 915 (2009).

[3] N. Nagaosa and Y. Tokura, Topological properties and dynamics of magnetic skyrmions, Nat. Nanotechnol. **8**, 899 (2013).

[4] B. Göbel, I. Mertig, and O. A. Tretiakov, Beyond skyrmions: Review and perspectives of alternative magnetic quasiparticles, Phys. Rep. **895**, 1 (2021).

[5] C. H. Marrows and K. Zeissler, Perspective on skyrmion spintronics, Appl. Phys. Lett. **119**, 250502 (2021).

[6] Y. Tokura and N. Kanazawa, Magnetic skyrmion materials, Chem. Rev. **121**, 2857 (2021).

[7] K. Everschor-Sitte, J. Masell, R. M. Reeve, and M. Kläui, Perspective: Magnetic skyrmions—Overview of recent progress in an active research field, J. Appl. Phys. **124**, 240901 (2018).

[8] C. Back, V. Cros, H. Ebert, K. Everschor-Sitte, A. Fert, M. Garst, T. Ma, S. Mankovsky, T. L. Monchesky, M. Mostovoy, N. Nagaosa, S. S. P. Parkin, C. Pfleiderer, N. Reyren, A. Rosch, Y. Taguchi, Y. Tokura, K. von Bergmann, and J. Zang, The 2020 skyrmionics roadmap, J. Phys. D **53**, 363001 (2020).

[9] G. Finocchio, F. Büttner, R. Tomasello, M. Carpentieri, and M. Kläui, Magnetic skyrmions: From fundamental to applications, J. Phys. D **49**, 423001 (2016).

[10] C. Zhang, C. Liu, S. Zhang, B. Zhou, C. Guan, Y. Ma, H. Algaidi, D. Zheng, Y. Li, X. He, J. Zhang, P. Li, Z. Hou, G. Yin, K. Liu, Y. Peng, and X.-X. Zhang, Magnetic skyrmions with unconventional helicity polarization in a van der Waals ferromagnet, Adv. Mater. **34**, 2204163 (2022).

[11] I. Kézsmárki, S. Bordács, P. Milde, E. Neuber, L. M. Eng, J. S. White, H. M. Rønnow, C. D. Dewhurst, M. Mochizuki, K. Yanai, H. Nakamura, D. Ehlers, V. Tsurkan, and A. Loidl, Néel-type skyrmion lattice with confined orientation in the polar magnetic semiconductor GaV_4S_8, Nat. Mater. **14**, 1116 (2015).

[12] C. Jin, C. Zhang, C. Song, J. Wang, H. Xia, Y. Ma, J. Wang, Y. Wei, J. Wang, and Q. Liu, Current-induced motion of twisted skyrmions, Appl. Phys. Lett. **114**, 192401 (2019).

[13] J. A. Garlow, S. D. Pollard, M. Beleggia, T. Dutta, H. Yang, and Y. Zhu, Quantification of mixed Bloch-Néel topological spin textures stabilized by the Dzyaloshinskii-Moriya interaction in Co/Pd multilayers, Phys. Rev. Lett. **122**, 237201 (2019).

[14] Y. Yuan, Z. Zeng, J. Wang, Y. Ma, S. Zhang, J. Wei, J. Wang, and Q. Liu, A skyrmion helicity-based multistate memory in synthetic antiferromagnets, J. Appl. Phys. **132**, 233903 (2022).

[15] K. Shibata, X. Z. Yu, T. Hara, D. Morikawa, N. Kanazawa, K. Kimoto, S. Ishiwata, Y. Matsui, and Y. Tokura, Towards control of the size and helicity of skyrmions in helimagnetic alloys by spin-orbit coupling, Nat. Nanotechnol. **8**, 723 (2013).

[16] C. Psaroudaki and C. Panagopoulos, Skyrmion qubits: A new class of quantum logic elements based on nanoscale magnetization, Phys. Rev. Lett. **127**, 067201 (2021).

[17] Z. Hou, Q. Zhang, X. Zhang, G. Xu, J. Xia, B. Ding, H. Li, S. Zhang, N. M. Batra, P. M. F. J. Costa, E. Liu, G. Wu, M. Ezawa, X. Liu, Y. Zhou, X. Zhang, and W. Wang, Current-induced helicity reversal of a single skyrmionic bubble chain in a nanostructured frustrated magnet, Adv. Mater. **32**, 1904815 (2020).

[18] J. Xia, X. Zhang, X. Liu, Y. Zhou, and M. Ezawa, Universal quantum computation based on nanoscale skyrmion helicity qubits in frustrated magnets, Phys. Rev. Lett. **130**, 106701 (2023).

[19] W. Wei, J. Tang, Y. Wu, Y. Wang, J. Jiang, J. Li, Y. Soh, Y. Xiong, M. Tian, and H. Du, Current-controlled topological magnetic transformations in a nanostructured kagome magnet, Adv. Mater. **33**, 2101610 (2021).

[20] S. A. Díaz and R. E. Troncoso, Controlling skyrmion helicity via engineered Dzyaloshinskii-Moriya interactions, J. Phys.: Condens. Matter **28**, 426005 (2016).

[21] B. Dai, D. Wu, S. A. Razavi, S. Xu, H. He, Q. Shu, M. Jackson, F. Mahfouzi, H. Huang, Q. Pan, Y. Cheng, T. Qu, T. Wang, L. Tai, K. Wong, N. Kioussis, and K. L. Wang, Electric field manipulation of spin chirality and skyrmion dynamic, Sci. Adv. **9**, eade6836 (2023).

[22] X. Z. Yu, K. Shibata, W. Koshibae, Y. Tokunaga, Y. Kaneko, T. Nagai, K. Kimoto, Y. Taguchi, N. Nagaosa, and Y. Tokura, Thermally activated helicity reversals of skyrmions, Phys. Rev. B **93**, 134417 (2016).

[23] J. Tang, Y. Wu, W. Wang, L. Kong, B. Lv, W. Wei, J. Zang, M. Tian, and H. Du, Magnetic skyrmion bundles and their current-driven dynamics, Nat. Nanotechnol. **16**, 1086 (2021).

[24] F. Zheng, F. N. Rybakov, A. B. Borisov, D. Song, S. Wang, Z.-A. Li, H. Du, N. S. Kiselev, J. Caron, A. Kovács, M. Tian, Y. Zhang, S. Blügel, and R. E. Dunin-Borkowski, Experimental observation of chiral magnetic bobbers in B20-type FeGe, Nat. Nanotechnol. **13**, 451 (2018).

[25] N. Kent, N. Reynolds, D. Raftrey, I. T. G. Campbell, S. Virasawmy, S. Dhuey, R. V. Chopdekar, A. Hierro-Rodriguez, A. Sorrentino, E. Pereiro, S. Ferrer, F. Hellman, P. Sutcliffe, and P. Fischer, Creation and observation of Hopfions in magnetic multilayer systems, Nat. Commun. **12**, 1562 (2021).

[26] J. Tang, Y. Wu, L. Kong, W. Wang, Y. Chen, Y. Wang, Y. Soh, Y. Xiong, M. Tian, and H. Du, Two-dimensional characterization of three-dimensional nanostructures of magnetic bubbles in Fe_3Sn_2, Natl. Sci. Rev. **8**, nwaa200 (2021).

[27] S. Zhang, G. Van Der Laan, J. Müller, L. Heinen, M. Garst, A. Bauer, H. Berger, C. Pfleiderer, and T. Hesjedal, Reciprocal space tomography of 3D skyrmion lattice order in a chiral magnet, Proc. Natl. Acad. Sci. USA **115**, 6386 (2018).

[28] W. Legrand, J.-Y. Chauleau, D. Maccariello, N. Reyren, S. Collin, K. Bouzehouane, N. Jaouen, V. Cros, and A. Fert, Hybrid chiral domain walls and skyrmions in magnetic multilayers, Sci. Adv. **4**, eaat0415 (2018).

[29] S. A. Montoya, S. Couture, J. J. Chess, J. C. T. Lee, N. Kent, D. Henze, S. K. Sinha, M.-Y. Im, S. D. Kevan, P. Fischer, B. J. McMorran, V. Lomakin, S. Roy, and E. E. Fullerton, Tailoring magnetic energies to form dipole skyrmions and skyrmion lattices, Phys. Rev. B **95**, 024415 (2017).

[30] L. Kong, J. Tang, W. Wang, Y. Wu, J. Jiang, Y. Wang, J. Li, Y. Xiong, M. Tian, and H. Du, Observation of hybrid magnetic skyrmion bubbles in Fe_3Sn_2 nanodisks, Phys. Rev. B **107**, 174425 (2023).

[31] G. L. Caer, B. Malaman, and B. Roques, Mossbauer effect study of Fe_3Sn_2, J. Phys. F **8**, 323 (1978).

[32] J. Tang, L. Kong, Y. Wu, W. Wang, Y. Chen, Y. Wang, J. Li, Y. Soh, Y. Xiong, M. Tian, and H. Du, Target bubbles in Fe_3Sn_2 nanodisks at zero magnetic field, ACS Nano **14**, 10986 (2020).

[33] I. Lyalin, S. Cheng, and R. K. Kawakami, Spin-orbit torque in bilayers of kagome ferromagnet Fe_3Sn_2 and Pt, Nano Lett. **21**, 6975 (2021).

[34] F. Zheng, H. Li, S. Wang, D. Song, C. Jin, W. Wei, A. Kovacs, J. Zang, M. Tian, Y. Zhang, H. Du, and R. E. Dunin-Borkowski, Direct imaging of a zero-field target skyrmion and its polarity switch in a chiral magnetic nanodisk, Phys. Rev. Lett. **119**, 197205 (2017).

[35] X. Zhao, C. Jin, C. Wang, H. Du, J. Zang, M. Tian, R. Che, and Y. Zhang, Direct imaging of magnetic field-driven transitions of skyrmion cluster states in FeGe nanodisks, Proc. Natl. Acad. Sci. USA **113**, 4918 (2016).

[36] A. Vansteenkiste, J. Leliaert, M. Dvornik, M. Helsen, F. Garcia-Sanchez, and B. Van Waeyenberge, The design and verification of MUMAX3, AIP Adv. **4**, 107133 (2014).

[37] W. Wang, JuMag – A Julia package for classical spin dynamics and micromagnetic simulations with GPU support, https://github.com/ww1g11/JuMag.jl.

[38] S. K. Walton, K. Zeissler, W. R. Branford, and S. Felton, MALTS: A tool to simulate Llorentz transmission electron microscopy from micromagnetic simulations, IEEE Trans. Magn. **49**, 4795 (2013).

[39] J. Tang, J. Jiang, N. Wang, Y. Wu, Y. Wang, J. Li, Y. Soh, Y. Xiong, L. Kong, S. Wang, M. Tian, and H. Du, Combined magnetic imaging and anisotropic magnetoresistance detection of dipolar skyrmions, Adv. Funct. Mater. **33**, 2207770 (2022).

[40] M.-G. Han, J. A. Garlow, Y. Liu, H. Zhang, J. Li, D. DiMarzio, M. W. Knight, C. Petrovic, D. Jariwala, and Y. Zhu, Topological magnetic-spin textures in two-dimensional van der Waals $Cr_2Ge_2Te_6$, Nano Lett. **19**, 7859 (2019).

[41] M. Heigl, S. Koraltan, M. Vaňatka, R. Kraft, C. Abert, C. Vogler, A. Semisalova, P. Che, A. Ullrich, T. Schmidt, J. Hintermayr, D. Grundler, M. Farle, M. Urbánek, D. Suess, and M. Albrecht, Dipolar-stabilized first- and second-order antiskyrmions in ferrimagnetic multilayers, Nat. Commun. **12**, 2611 (2021).

[42] D. Chakrabartty, S. Jamaluddin, S. K. Manna, and A. K. Nayak, Tunable room temperature magnetic skyrmions in centrosymmetric kagome magnet Mn_4Ga_2Sn, Commun. Phys. **5**, 189 (2022).

[43] Y. He, T. Helm, I. Soldatov, S. Schneider, D. Pohl, A. K. Srivastava, A. K. Sharma, J. Kroder, W. Schnelle, R. Schaefer, B. Rellinghaus, G. H. Fecher, S. S. P. Parkin, and C. Felser, Nanoscale magnetic bubbles in $Nd_2Fe_{14}B$ at room temperature, Phys. Rev. B **105**, 064426 (2022).

[44] M. Schmitt, T. Denneulin, A. Kovács, T. G. Saunderson, P. Rüßmann, A. Shahee, T. Scholz, A. H. Tavabi, M. Gradhand, P. Mavropoulos, B. V. Lotsch, R. E. Dunin-Borkowski,

Y. Mokrousov, S. Blügel, and M. Kläui, Skyrmionic spin structures in layered Fe_5GeTe_2 up to room temperature, Commun. Phys. **5**, 254 (2022).

[45] J. C. Loudon, A. C. Twitchett-Harrison, D. Cortés-Ortuño, M. T. Birch, L. A. Turnbull, A. Štefančič, F. Y. Ogrin, E. O. Burgos-Parra, N. Bukin, A. Laurenson, H. Popescu, M. Beg, O. Hovorka, H. Fangohr, P. A. Midgley, G. Balakrishnan, and P. D. Hatton, Do images of biskyrmions show type-II bubbles? Adv. Mater. **31**, 806598 (2019).

[46] S.-G. Je, H.-S. Han, S. K. Kim, S. A. Montoya, W. Chao, I.-S. Hong, E. E. Fullerton, K.-S. Lee, K.-J. Lee, M.-Y. Im, and J.-I. Hong, Direct demonstration of topological stability of magnetic skyrmions *via* topology manipulation, ACS Nano **14**, 3251 (2020).

[47] See Supplemental Material at http://link.aps.org/supplemental/10.1103/PhysRevB.109.014401 for figures for simulated helicity for top, middle, and bottom layers in the mutual transformation of C1-C3-C2-C4; simulated comparison of magnetic structures with initial and thermal after 1 ns at $t = 300$ K for C1 and C3 skyrmions; simulated average in-plane magnetization mappings for magnetic structures initialized with C1 and C3 skyrmions at varying thicknesses; simulated in-plane magnetization mappings and corresponding under-defocused fresnel images of the C3 and C4 skyrmion in different depth regions; simulated 3D magnetic structure and corresponding under-defocused fresnel images in the bubble-to-skyrmion transformation at $b \sim 200$ mT with decreasing field angle β; simulated helicity for top, middle, and bottom layers in dipolar skyrmion transformation with increasing magnetic field at a field angle $\beta = 0$; and simulated 3D dipolar skyrmions of four hybrid configurations.

[48] J. Tang, L. Kong, W. Wang, H. Du, and M. Tian, Lorentz transmission electron microscopy for magnetic skyrmions imaging, Chin. Phys. B **28**, 087503 (2019).

[49] T. Matsumoto, Y.-G. So, Y. Kohno, H. Sawada, Y. Ikuhara, and N. Shibata, Direct observation of Σ7 domain boundary core structure in magnetic skyrmion lattice, Sci. Adv. **2**, e1501280 (2016).

[50] D. McGrouther, R. J. Lamb, M. Krajnak, S. McFadzean, S. McVitie, R. L. Stamps, A. O. Leonov, A. N. Bogdanov, and Y. Togawa, Internal structure of hexagonal skyrmion lattices in cubic helimagnets, New J. Phys. **18**, 095004 (2016).